Thermocapillary flow in drops under low gravity analysed by the use of liquid crystals

M. Treuner, H. J. Rath, U. Duda, J. Siekmann

Abstract Thermocapillary flow within large sized drops of diameters up to 15 mm was studied experimentally during KC-135 parabolic flights. For the simultaneous observation of the flow and the temperature fields inside the drops, visualisation by means of liquid crystal tracers was applied. Due to the curved surfaces of the drops, a special evaluation method has to be taken into account. The experimental set up and the test procedure as well as a qualitative description of the observed flow behaviour in high Prandtl number liquids are described.

List of symbols

a	thermal diffusivity
Bo_{dyn}	dynamical Bond number, Eq. (4)
g	acceleration
g_o	acceleration due to gravity on earth
Gr	Grashof number, Eq. (5)
H	distance between the stemples
Ma	Marangoni number, Eq. (2)
m	order of reflected wavelength
n	refractive index
n_{21}	refractive index ratio of medium 1 related to medium 2
P_i	point where P_r is imaged
P_k	intersection point between light sheet beam and drop surface
P_l	point on the symmetry axis
P_r	point with real coordinates in the light-sheet plane
P_s	intersection point between observation beam and drop surface
Pr	Prandtl number, Eq. (3)
R	drop radius
Re_M	Reynolds number Eq. (1)
r_i	radial coordinate at the image
r_r	real radial coordinate in the light-sheet plane
$S(x)$	function of the drop shape
$S'(x)$	derivative dS/dx
ΔT	maximum temperature difference applied to the drop
T	temperature
T_w	temperature at the warm stemple
T_k	temperature at the cold stemple
u_r	backflow velocity in the core region
U_M	characteristic Marangoni velocity
$\vec{V}_L$	light sheet beam in the drop
$\vec{V}_B$	reflected beam in the drop
x	axial coordinate of the drop
x_i	imaged axial coordinate on the flow picture
x_r	real axial coordinate
y	coordinate normal to x and z axis
y_i	imaged y-coordinate on the flow picture
y_r	real y-coordinate in the light-sheet plane
z	coordinate in observation direction

Greek letters

α	reflection angle in fluid 2
β	reflection angle in fluid 1, thermal expansion coefficient
ε	inclination angle between observation axis and light-sheet plane
η	dynamic viscosity
λ	heat conductivity
φ	reflection angle on the crystal's surface
v	kinematic viscosity
ρ	density
σ	surface tension
$\partial\sigma/\partial T$	temperature dependence of the surface tension
ξ	angle in the light-sheet plane, Eq. (8)

M. Treuner, H. J. Rath
ZARM, Universität Bremen, D-28334 Bremen,
F.R. Germany

U. Duda, J. Siekmann
Lehrstuhl für Mechanik, Universität-GH-Essen,
D-45127 Essen, F.R. Germany

Correspondence to: M. Treuner

1
Introduction

Thermal gradients along liquid surfaces cause fluid motions due to the temperature dependence of the surface tension. This gravity independent flow mechanism gives rise to basic heat and mass transfer mechanisms in numerous technological processes involving liquid-gas interfaces. Let us mention e.g.

solidification front dynamics or welding processes. Especially during containerless material processing under low gravity conditions, thermocapillary convection plays a major role. Under terrestrial conditions thermocapillary convection is superimposed by buoyancy effects. The unmasked effect of thermocapillary flow can only be observed under low gravity conditions.

The present literature focusses on theoretical and experimental considerations of idealised geometrical configurations like cylindrical liquid bridges or square cavities, which represent existing crystal growth technologies, (cf. Schwabe 1981). Several publications describe the theoretical investigations of thermocapillary flows in spherical drops, e.g. Jayaraj et al. (1982), Bauer (1982), Bauer and Eidel (1987), Saghir and Choma (1987), Petri (1990) and Petri et al. (1991). All these publications describe two-dimensional steady-state flows and assume a given steady temperature field as boundary condition on the free surface.

Since thermocapillary flows are characterized by the coupling of the flow fields and the temperature fields, a visualization method for their simultaneous observation was requested. The application of liquid crystals as tracer particles was proved adequate in many cases, e.g., Hiller and Kowalewski (1987). Since the wavelength reflected by the tracer particles strongly depends on the angle of reflection, a quantitative evaluation of the observed temperature fields has been carried out only in simple geometries using plane windows. To evaluate the flow behaviour at the curved surfaces of drops the characteristics of the tracer particles' image is studied here.

The basic similarity analysis for thermocapillary flows has been given by Ostrach (1982) and Napolitano et al. (1985). The steady state flow case is governed by two dimensionless numbers, the Reynolds number (Eq. (1)), which is defined with the Marangoni velocity U_M, or alternatively the Marangoni number (Eq. 2), and the Prandtl number (Eq. (3)).

$$Re_M = \frac{U_M \cdot R}{v} \quad \text{with} \quad U_M = \left|\frac{\partial \sigma}{\partial T}\right| \cdot \frac{\Delta T}{\eta}, \quad (1)$$

$$Ma = \frac{U_M \cdot R}{a}, \quad (2)$$

$$Pr = \frac{v}{a}. \quad (3)$$

For an estimation of the dominance of thermocapillary forces, the dynamical Bond number can be applied (Eq. (4)), which is defined as the ratio of buoyancy forces, represented by the Grashof number (Eq. (5)), to thermocapillary forces, given by Re_M. If the acceleration vanishes ($g \rightarrow 0$), the dynamical Bond number tends to zero.

$$Bo_{\mathrm{dyn}} = \frac{Gr}{Re_M} = \frac{\rho \cdot g \cdot \beta \cdot R^2}{\left|\frac{\partial \sigma}{\partial T}\right|} \quad (4)$$

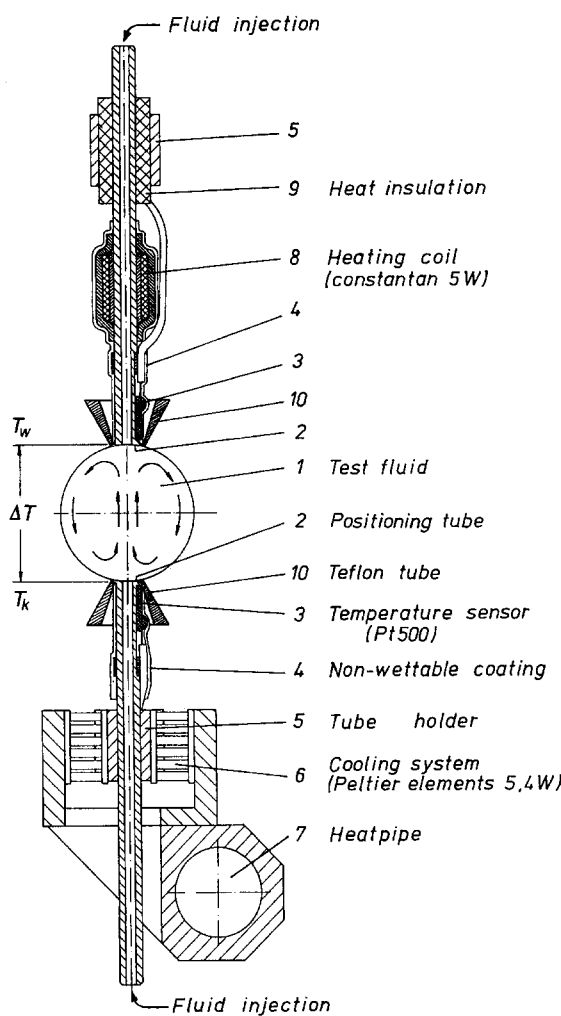$$Gr = \frac{g \cdot \beta \cdot \Delta T \cdot R^3}{v^2} \quad (5)$$

Fig. 1. Experimental drop environment

2
Experimental setup an procedure

2.1
Experimental fluid handling

The experiments were carried out on parabolic flights with a residual average acceleration of $10^{-2}\,g_0$ and a duration time of up to 25 seconds. Figure 1 shows the positioning system to fix the drop in the test section. It consists of two wettable open tubes, equipped with sharp, acute edges. The construction allows the drop shape and the contact angle at the edges to adapt to the slightly varying gravity level g. The dynamic stability of such a spherical liquid bridge depends on the drop and the tube diameter, the surface tension, the density, the viscosity of the liquid and on the acceleration. For the typical g-jitter disturbances occurring during parabolic flights and the liquids used (see Chap. 2.3), an adequate ratio of the drop diameter to the tube diameter was found at a value of three. Behind the edges the tubes were covered with teflon cones (10), to protect wetting in the case of strong µg-disturbances.

Temperature gradients were applied to the drop by heating the upper tube with a heating coil (8) and cooling the lower one with Peltier-elements (6). Temperature sensors (3) were implemented close to the wetted areas. In order to enable fast

changes of the temperatures, the tubes were designed with minimized heat capacity. A fast variation of the tube temperatures was necessary owing to the narrow temperature range in which the liquid crystals were active.

The drops were created by injection through the tubes. Typical acceleration profiles of the plane start with an residual acceleration in direction of the cold tube. Due to that, injection only through the upper warm tube was the most convenient way of drop generation, as practiced in most of the cases. The fluid dosimetrie was managed by a precision syringe driven by a stepping motor. A heat exchanger preheated the fluid to a certain temperature before injection. An optimized coordination as well as data recording was controlled by the use of a processing computer.

2.2
Optical arrangement

As mentioned previously the selective temperature dependent spectral reflection of cholesteric liquid crystal tracers was used for simultaneous visualization of the flow and the temperature fields. Figure 2 shows the optical arrangement. In order to illuminate the drops, a light-sheet supplied by a Xenon-lamp (300W, Cermax), was employed. Two photo-cameras (A and B) documented the observed flow in multiple exposure technique from different angles. The observation axis of camera A was arranged normal to the light sheet plane, camera B was turned to an angle of 50°. It will be shown in Chap. 3.2, that both perspectives lead to different possibilities of observation. Axis A is advantageous for the inner bulk volume, Axis B for the vicinity of the free surface. An additional CCD-camera recorded the dynamical flow behaviour in order to document the direction of motion of the tracers on the photographs. Observation of the drop generation process was achieved by changing to a diffuse illumination.

2.3
Test fluids and procedure

The liquids used in the experiment were glycerol/water-solutions with mass fractions of 80% and 87% glycerol. As a criterion for the selection chemical resistance with the liquid crystals and nearly the same density were required. The high
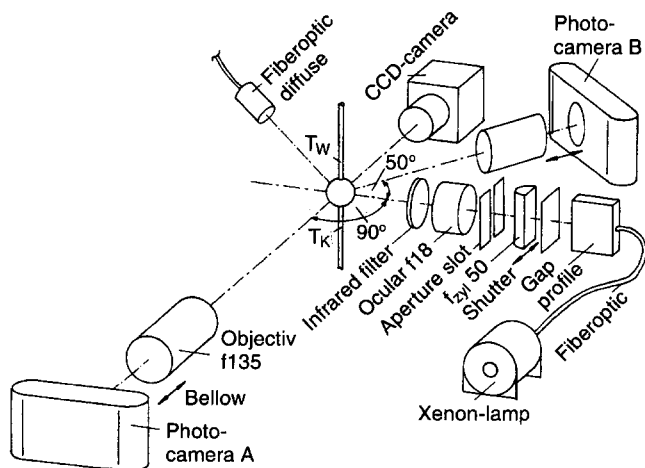
Table 1. Physical data of the test fluids

Physical quantity	Reference temperature T[°C]	Glycerol mass fraction 80%	Glycerol mass fraction 87%
ρ [10^3 kg/m^3]	25	1.206	1.224
	30	1.202	1.222
	35	1.200	1.218
v [10^{-6} m^2/s]	25	40.4	92.5
	30	29.2	63
	35	18.0	34
η [10^{-3} kg/ms]	25	48.7	114
	30	35.1	77
	35	21.5	40
λ [W/mK]	25	0.332	0.312
	30	0.333	0.313
	35	0.335	0.314
a [10^{-6} m^2/s]	25	0.105	0.101
	30	0.105	0.102
	35	0.106	0.102
σ [10^{-3} N/m]	25	64.0	62.5
	30	63.6	62.1
	35	63.2	60.9
n	25	1.443	1.445
	30	1.442	1.453
	35	1.441	1.452
β [1/K]	25	0.467	0.474
	30	0.465	0.473
	35	0.464	0.471
$\partial\sigma/\partial T$ [10^{-3} N/mK]	25	−0.08	−0.08
	30	−0.08	−0.08
	35	−0.08	−0.08

viscosity was found ideal to withstand the typical micrograivity disturbances on the parabolic flights, but at the same time limited the investigation to high Prandtl numbers with average values between $Pr = 280$ and $Pr = 700$. The physical properties of the test fluids are given in Table 1. In order to check changes of the surface tension, the fluids with the liquid crystals were controlled with the ring method. No influence on the surface tension gradient was observed within the limits of the measurement accuracy ($\Delta(\partial\sigma/\partial T)\pm 0.01\cdot 10^{-3}$ N/mK).

Three different drop geometries were generated. With wetting contact to both positioning tubes, completely spherical drops with diameters $D = 13$ mm and $D = 15$ mm were generated, as well as oval-shaped drops with the same length but a reduced volume of 80%. In addition drops, positioned with only one tube, were generated with several diameters between $D = 9$ mm and $D = 12$ mm. With regard to the average acceleration level of $10^{-2} g_0$, the dynamical Bond number was in the range between $Bo_{dyn} = 0.016$ and $Bo_{dyn} = 0.082$.

The injected liquid was preheated to a temperature of 26.6 °C where the liquid crystals start reflecting with red colour. Temperature differences with values of up to $\Delta T = 45$ K were applied to the drops. For the drop configurations with wetting on both positioning stemples, the corresponding

Fig. 2. Optical arrangement

dimensionless parameters are ranging between $Re_M = 4.1$ and $Re_M = 39.8$, respectively $Ma = 2653$ and $Ma = 8346$. In the case of the drops, positioned with a single stemple, the respective values are $Re_M = 3.9$ up to $Re_M = 12.1$ and $Ma = 1966$ up to $Ma = 3617$.

3
Evaluation of the test data

3.1
Fundamental optical situation

For evaluation of the optical image of a single tracer particle in the illuminated cross-section plane of the drop, two principal effects have to be taken into account. On the one hand, the spatial image of the tracer particles is distorted by the refraction at the drop's surface. On the other hand, the selective reflection (colourplay) of the liquid crystals depends on their temperature and also on the angle of reflection. Since the colour of the tracer particle is intended to indicate the temperature, the angle and the temperature dependence have to be considered.

Figure 3 illustrates the typical optical situation. We restrict the explanation to the case, when the beams are refracted in the depicted plane. A beam of the light sheet propagates into the drop and is reflected by a crystal under a certain angle 2φ. The outgoing beam then is refracted at the drops surface, as characterized by the angles α and β. Refraction is described by the Snellius law (Eq. (6)).

$$\sin(\alpha) = n_{21} \cdot \sin(\beta). \tag{6}$$

The temperature dependence of the selective reflection is a specific feature of the liquid crystals' periodic helical structure. The wavelength λ, reflected parallel to the helical axis, is proportional to the spatial period q_0 between the twisted layers. For crystals with a homogeneous chemical composition, q_0 is a function of the temperature. A complete description of the optical properties can be found in De Gennes and Prost
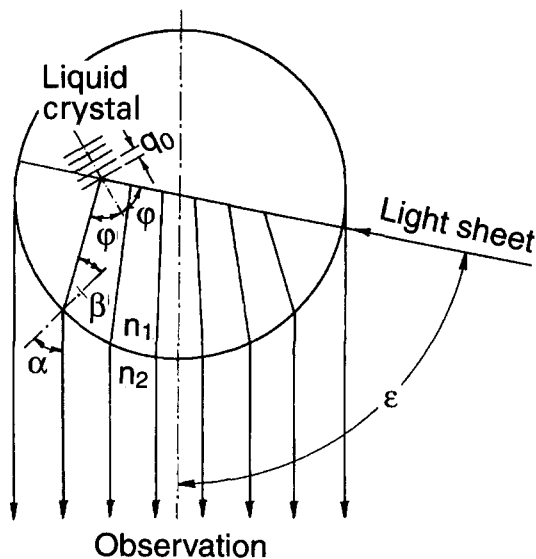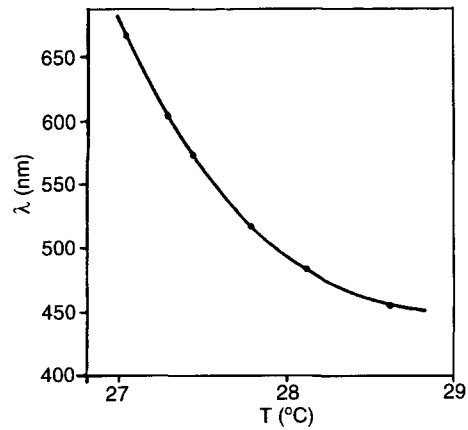

Fig. 4. Calibration curve of the selective reflection of liquid crystals TM107, BDH Chemicals Ltd., (Hiller and Kowalewski 1989)

(1993). They described the angular dependence of the selective reflection of cholesteric liquid crystals as a Bragg reflection. The reflected wavelength λ is given by (Eq. (7)); m is the order of reflection and $\bar{n}$ is the average refractive index of the liquid crystals.

$$q_0 \cdot \cos \varphi = \frac{m \cdot \lambda}{\bar{n}}. \tag{7}$$

The smaller the reflection angle φ, the longer is the reflected wavelength λ. With the observation of a real three-dimensional configuration, like spherical drops, φ varies in a wide range. If the inclination angle ε between the light-sheet plane and the observation axis varies, the image changes considerably. Both effects, optical distortion and shift of the wavelength, have to be taken into account for the evaluation of the tracer particles. Their effect on the image of the inner cross section area in spherical drops is presented in Chap. 3.2.

The calibration curve of the type TM107 (BDH Chemical Ltd.), suspended in glycerol, was documented by Hiller and Kowalewski (1987) and is shown in Fig. 4. The dependence of the reflected wavelength λ on the temperature was measured under an angle of 90° with respect to the direction of the incident light. When suspended in the liquid, the tracers are transparent above and below a certain temperature range. The microencapsulated type used here starts reflecting with white colour at 25 °C, passes the colour spectrum from red, green, yellow to blue between 26.5 °C and 29 °C, reflects white until 32°C, and then is again transparent. Observation under different angles leads to different results.

To restrict the optical situation three assumptions were made:

● The drop surface is assumed rotationally symmetric, with the x-axis being the axis of symmetry.
● The observation distance is sufficiently large to consider the outgoing beams as parallel to the z-axis.
● The beams of the light sheet are parallel, before they propagate into the drop.

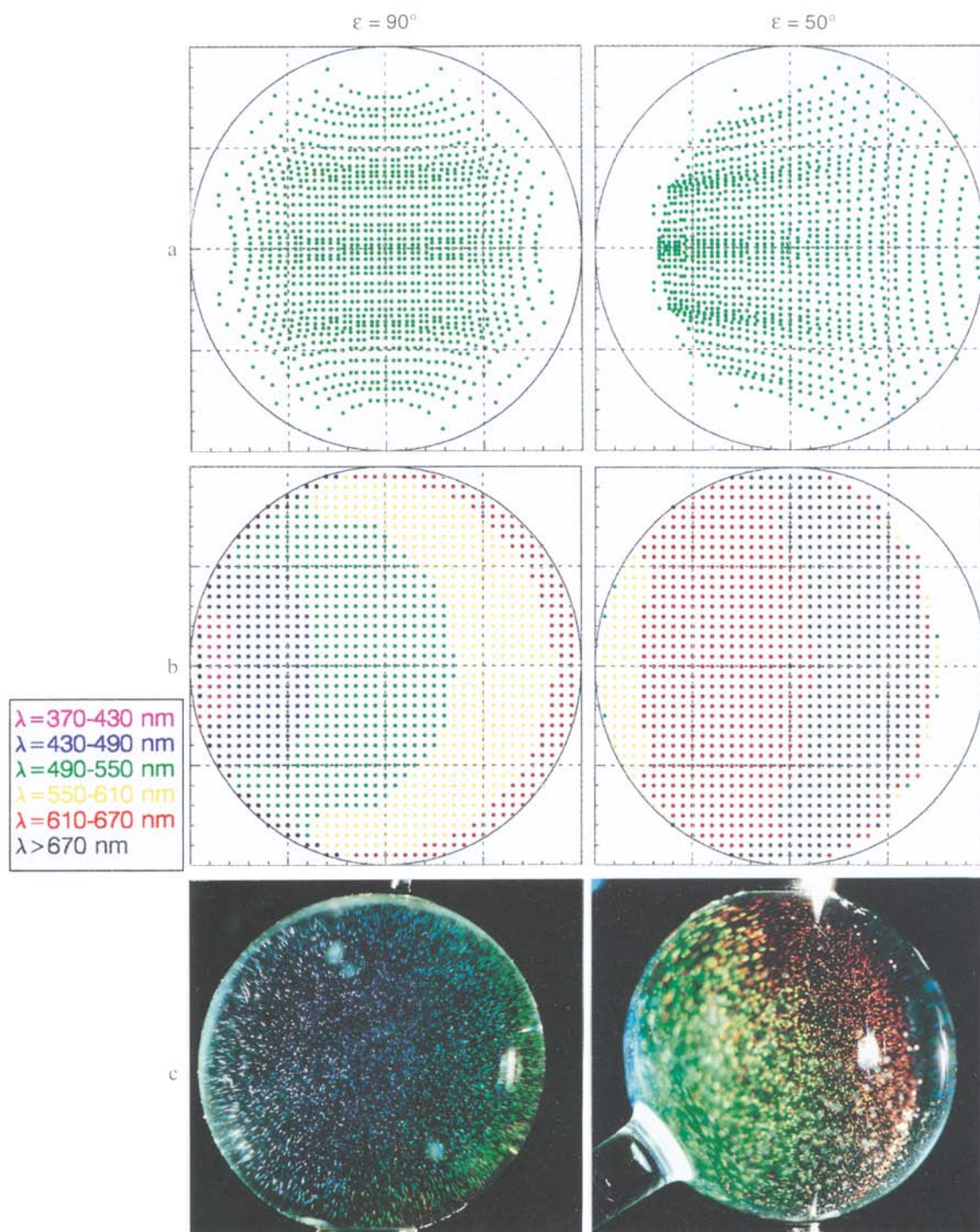The geometrical configuration, as considered for the evaluation, is shown in Fig. 5.

Fig. 3. Fundamental optical situation

Fig. 5. Geometrical arrangement for the optical transformation

3.2
Spatial image of the light sheet plane

For the quantitative evaluation of the flow fields, only the spatial distortion has to be taken into account. A relation was found for the transformation of the real coordinates in the illuminated cross section plane and the corresponding coordinates in the virtual image.

In Fig. 5, the drop is depicted shaped ovally, with the symmetry axis along the x-axis. In order to observe under different angles, the light-sheet is variably inclined against the x, z-plane with an angle ε. The shape of an arbitrary, rotationally symmetrical surface is given by a function $S(x)$. The real position of a point P_r in the light-sheet plane appears in the virtual image at point P_i. The observation beam intersects the surface of the drop in point P_s, where the beam is refracted according to the Snellius law (Eq. (6)). Point P_l is given by the intersection point of the normal vector in point P_s with the symmetry axis. The coordinates x_r and y_r of point P_r are given by the intersection of the observation beam with the connecting line between P_l and P_i in the light-sheet plane. The complete relations used for the optical transformation are given by (Eq. (8–12)).

$$x_r = x_L + \overline{P_l P_r} \cdot \text{sgn}(x_i) \frac{y_i}{\sqrt{\sin \varepsilon \cdot (x_i - x_l)}} \tag{8}$$

$$y_r = \overline{P_l P_r} \cdot \text{sgn}(y_i) \frac{y_i}{\sqrt{\sin \varepsilon \cdot (x_i - x_l)}}, \tag{9}$$

$$\overline{P_l P_r} = \frac{\sin \alpha \cdot \sqrt{(x_i - x_l)^2 + S(x_i)^2}}{n_{21} \cdot \sin\left(\pi - \arcsin\left(\frac{\sin \alpha}{n_{21}}\right) - \arcsin\left(\frac{\sin \alpha \left(\left|\sqrt{S(x_i)^2 - y_i^2}\right| - \frac{y_i}{\tan \varepsilon}\right)}{\sqrt{(x_i - x_l)^2 + \left(\frac{y_i}{\sin \varepsilon}\right)^2}}\right)\right)} \tag{10}$$

$$\alpha = \arccos \frac{\sqrt{S(x_i)^2 - y_i^2}}{\sqrt{(x_i - x_l)^2 + S(x_i)^2}}, \tag{11}$$

$$x_l = x_i + S(x_i) \cdot S'(x_i). \tag{12}$$

In the case of a completely spherical drop and an observation angle of $\varepsilon = 90°$, optical distortion occurs only in radial direction. If cylindrical coordinates are chosen, the radius could be corrected by the simplier equation (13).

$$r_r = \frac{r_i}{n_{21} \cdot \sin\left(\frac{\pi}{2} + \arcsin\left(\frac{r_i}{R}\right) - \arcsin\left(\frac{r_i}{R \cdot n_{21}}\right)\right)}. \tag{13}$$

The characteristic image in spherical drops, together with the spectral dispersion of the reflected light is given as an example in Fig. 6.

3.3
Spectral dispersion of the reflected light

For determining the reflected wavelengths by means of the Braggs law (Eq. (7)), the optical analysis has to be extended to the beam paths of the light sheet. They were assumed to be parallel and orthogonal to the symmetry axis before entering the drop. On the drop's surface a single beam is refracted in point P_k, then propagates into the drop, and reflects at the surface of a liquid crystal in point P_r. The outgoing beam then propagates as described in Chap. 3.1. The angle 2φ between in- and outgoing beam can be determine by the product of the describing vectors and is given by (Eq. (14)). Since the coordinates of point P_k, (x_k, y_k, z_k), could not be derived analytically, they were determined numerically by an iteration routine:

$$\varphi = 0.5 \cdot \arccos\left(\frac{\vec{V}_L \cdot \vec{V}_B}{|\vec{V}_L| \cdot |\vec{V}_B|}\right)$$

with $\quad \vec{V}_L = (x_s - x_r, y_s - y_r, z_s - z_r)$

$$\vec{V}_B = (x_k - x_r, y_k - y_r, z_k - z_r) \tag{14}$$

In order to make evident the characteristics of the optical image in spherical drops, an example is given in Fig. 6. The virtual image is depicted for $\varepsilon = 90°$ and $\varepsilon = 50°$. Figure 6a represents the real location of the points in the illumination plane, which render the linear grid in the virtual image of Fig. 6b. The drop in the example given is spherical with radius one, the refractive indices correspond to a 80% glycerol/water-mixture ($n_{21} = 1.442$), and the average refractive index for the liquid crystals is $\bar{n} = 1.47$. At a temperature of 27.25°C and a reflection angle of $2\varphi = 90°$, the crystals reflect the wavelength $\lambda = 500$ nm, according to the spatial period q_0 of their helical structure. This value was assigned to an isothermal liquid, presented with green colour in Fig. 6a. The wavelengths arising in the virtual image are depicted with false colours in Fig. 6b, describing equal wavelength intervals. Photographs of isothermal hollow spheres, filled with the above liquid, are shown in Fig. 6c for a comparison of the results. In all the

Fig. 6. Image and shift of the reflected wavelength in the cross-section of spherical drops

representations of Fig. 6, the light-sheet is orientated horizontally and appears from the right.

It becomes evident in Fig. 6a, that especially the image of the cross-sectional area in the vicinity of the drop's edge changes rapidly with the observation angle ε. At $\varepsilon = 90°$ the inner area is imaged with approximately constant magnification. Up to the edge of the cross-section, the image is rapidly compressed in radial direction and leads to undesired restrictions for the observation. Only a limited area of the cross-section is imaged

under an angle of $\varepsilon = 50°$, but the drop's periphery, where the light-sheet enters, is observable.

In comparison to the wavelength $\lambda = 50$ nm reflected under $2\varphi = 90°$, the observed wavelengths are shifted to larger values on the right part of the cross-section and to smaller values on the left side. Like in the real photographs, the regions of equal shift occur with crescent shape under both observation angles. At $\varepsilon = 90°$, the maximum theoretical difference of the wavelength between left and right edge of the drop is

$\Delta\lambda = 224$ nm. If the transition to yellow coloured particles on the right edge is ascribed with $\lambda = 580$ nm and the colourless ones on the left edge with $\lambda = 370$ nm, the resulting difference of $\Delta\lambda = 210$ nm confirms the theoretical result very well. At $\varepsilon = 50°$, the theoretical value for the maximum difference is $\Delta\lambda = 107$ nm. With $\lambda = 600$ nm for the red colour on the right edge and $\lambda = 480$ nm for indigo on the left edge, the difference of $\Delta\lambda = 120$ nm as well corresponds theory. Compared to the observation under 90°, the spectrum of the reflected light under an angle of 50° is more narrow, but shifted to larger wavelengths.

3.4
Evaluation of the flow pictures

The argument between the theoretical description and the experimental findings in Fig. 6 renders to a useful description of the optical images. Though the interpretation of the colours depends on the individual perception of the viewer, here only the qualitative findings were used to discuss the temperature behaviour.

The observed flow fields were documented on the photographs in multiple exposure technique. In order to determine the flow behaviour quantitatively, the tracers' paths were optically corrected as described in Chap. 3.1. Evaluation was carried out by means of a personal computer. All the data like the drop shape and the tracers' coordinates were manually read in with a digitising tablet from amplified prints. In order to check the accuracy of the applied velocity measurement, simulation experiments have been carried out in density matched fluid systems under normal gravity by Duda (1983). The error of the velocities has been found to be less than 5%.

4
Experimental results and discussion

As mentioned in Chap. 2.1., drop generation and positioning worked very satisfactorily considering to the conditions of the parabolic manoeuvres. In about 180 parabolas, over 75% of the generated drops could be held between the tubes for more than 15 seconds. On the other hand, the creation of the desired flow pictures was more problematically. Already a short gravity-peak one order of magnitude larger than the average level, was able to ruin a multiple exposure picture. Parts of the experiments failed, due to that. Nevertheless, thermocapillary convection was successfully induced and documented on numerous satisfactoring flow pictures. The evaluation and description of the observed flow patterns is demonstrated with two examples.

Figure 7 presents a sequence of four pictures of an oval-shaped drop with an 80% glycerol solution. The drop is heated from the warm stemple at the upper margin and cooled from the cold one below. The visible flow in the bulk is from the cold to the warm pole. The image of the flow on the surface and in the surface near areas, which is driven in the direction of descreasing temperature by the surface tension, isn't visible due to the preceding considerations.

The pictures were taken in intervals of 2.1 s. Each was exposed three times with 0.25 s and 0.25 s interruption time. The slightly winded tracer paths document typical vibrational distortions ($f \approx 3$ Hz), which are transferred to the light path. The exposed pathlines on the photographs occur in a curved manner. Since the whole drop (as a relative system for single tracer-particles) underlies these vibrations, the curvature of the single exposure lines can be neglected. Pathlength and flow direction were determined by a linear interpolation of three partial-exposures of the same tracer. As an example for the evaluation, the tracers from Fig. 7d are depicted after the optical correction in Fig. 7e.

Since the drops were generated by injection through the upper warm stemple, the desired temperature difference is reduced in the beginning of the parabola. It increases from picture to picture. The corresponding parameters of Fig. 7 are listed in Table 2.

Though steady state flow could not be observed in the experiments, the development of the flow field may be interpreted as quasi steady state flow behaviour. The characteristical momentum diffusion time R^2/v is 1.45 seconds. Due to that the flow field gets stationary within a few seconds. On the other hand, the corresponding temperature diffusion time R^2/a is 4.7 minutes, which means a slow approach to a steady state temperature field.

The time dependence, however, becomes obvious from the colourplay of the tracer-particles. Starting from Fig. 7a, the dark inner volume in the core of the drop indicates temperatures below 26.5 °C. The outer volume with blue colour indicates an area with temperatures $T > 28$ °C. Due to the flow induced by the thermocapillary forces, heat is transferred along the surface from the warm pole to the cold pole and by the backflow in the bulk by both convection and conduction. This principle behaviour is sketched by the development of an isotherm in Fig. 7f. As it can be seen by the development in the actual sequence, the isotherms were swept towards the cold area by the convective heat transport. The backflow of the cooler fluid in the bulk pushes the isotherms upwards. The region around the cold pole becomes smaller and moves upwards in direction of the warm region above. Thus, the increasing average temperature in the drop becomes evident.

Figure 8 presents the typical case of a spherical drop (87% glycerol, $D = 13$ mm), observed under different angles ε. The temperature difference, heated from above, was $\Delta T = 39.2$ K. From the above investigations it is evident that both views appear with a strongly different colour spectra. Whereas the tracers in the cold inner region reflect with white colour in Fig. 8a, they are invisible in Fig. 8b. The colours are reflected with a narrower spectrum but shifted to larger wavelengths when observed under an angle of $\varepsilon = 50°$. This becomes distinctive at the transition from the dark (cold) inner region to the warmer blue region on the drops periphery. The temperature field there is imaged with a higher resolution, but indicates lower temperatures according to the calibration curve in Fig. 4.

The temperature conditions on the free surface are the key for the analysis of thermocapillary flows. In both perspectives of Fig. 8, the drop's periphery is imaged with constant colour. From the above theoretical description, we know that the colour shift in that region is approximately constant, too. As far as the colour image is not hidden by reflections, as in the vicinity of the positioning tubes, the temperature appears to be constant over the main parts the drop's surface. Due to the convection, strong gradients along the surface only occur close to the positioning tubes. This behaviour is characteristic for thermocapillary flow in high Prandtl number liquids and is
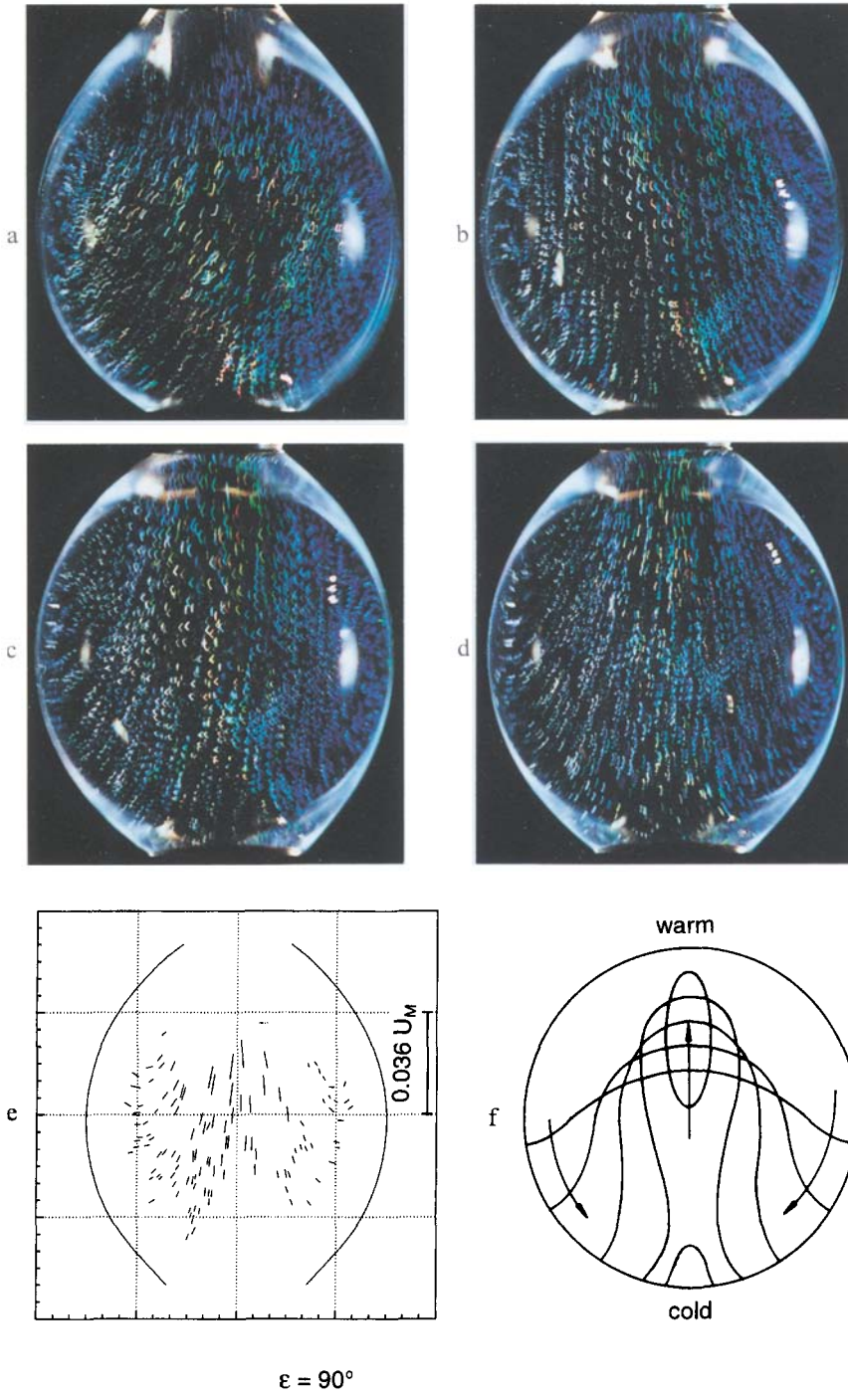
ε = 90°

ε = 50°

Fig. 7. Time dependent development of the thermocapillary flow in an oval-shaped drop
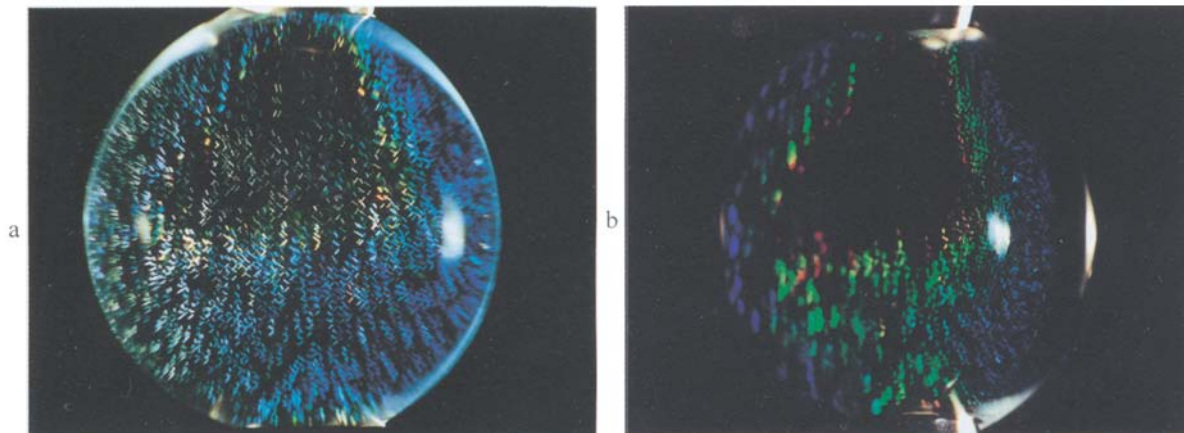
Fig. 8. Visualized flow field in a spherical drop under different observation angles

Table 2. Parameters of the thermocapillary flow in Fig. 7

Figure 7	temperature difference ΔT [K]	reference velocity U_M [m/s]	average Prandtl number $Pr = 280$	
			Re_M	Ma
(A)	34.4	0.07841	17.5	4853.6
(B)	39.0	0.08889	19.8	5502.6
(C)	41.9	0.09550	21.3	5911.8
(D)	44.5	0.10994	26.5	6806.1
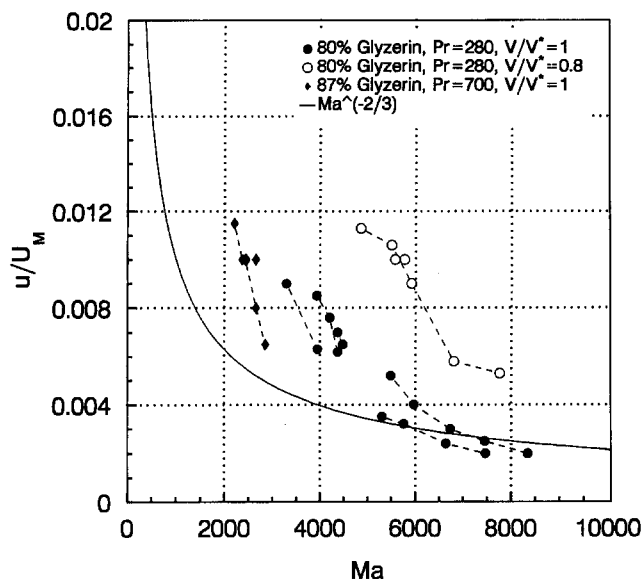
Fig. 9. Marangoni number dependence of measured velocities in the center of the drops

generally confirmed by theoretical analyses, e.g. Carpenter and Homsy (1990).

Though the observation under an angle of 50° was intended to document the velocity distribution on the drop's periphery, the tracers in that area are slightly blurred in Fig. 8b. The µg-disturbances here negatively affected the depth of the field. From amplified prints we found the surface velocities to be approximately 50% of the backflow velocities in the bulk volume. Restrictions have to be made for the vicinity of the stemples, where due to reflexions no evaluation was possible.

In order to characterise the measured velocities in dependence on the Marangoni number, several cases are compared in Fig. 9. The velocities were measured in the centre of the drops.

The values obtained with the same drop in one parabola are connected by a dashed line. Since the temperature difference applied increases during the measured periods, the Marangoni number increases too. In all the cases, the dimensionless velocities are showing the same decreasing dependence on the increasing Marangoni number. Three principle parameters have to be distinguished in Fig. 9, like the case of spherical liquid bridges with 80% ($\overline{Pr} = 280$), or 87% solutions ($\overline{Pr} = 700$), or the case of oval-shaped liquid bridges

characterised by their volume V, related to the volume of a completely spherical one V^*. An order of magnitude analysis of Napolitano et al. (1985), (Eq. (15)), is depicted in the diagram for comparison. Their results are valid for the core volume of thermocapillary flow in liquid bridges and confirm the assumption of a quasi-steady time dependent development of the observed flow fields.

$$\frac{u_r}{U_M} \approx Ma^{-2/3} \tag{15}$$

However, quantitative comparison of the flow behaviour measured in spherical drops with the theoretical considerations mentioned in the introduction failed referring to one point. The temperature boundary conditions assumed as a given steady distribution in the theoretical models were found to be incomparable to the temperature distribution observed in the experiments. This may explain that the velocities predicted e.g. by Petri et al. (1991) are 10 to 15 times larger than the values observed in the experiments.

4
Conclusion

Thermocapillary convection in drops was investigated experimentally under low gravity, using parabolic flights. A simultaneous visualisation of the flow and the temperature fields was successfully achieved by means of liquid crystal tracers. The fundamental optical features of the image at the curved drop surface are described and a proper evaluation method is presented. The dispersion of the wavelength reflected into the direction of observation is in general agreement with the experimentally observed image. The thermocapillary flow behaviour observed for high Prandtl number liquids was analysed and discussed.

References

Bauer HF (1982) Marangoni convection in a freely floating liquid sphere due to axial temperature fields. Ingenieur-Archiv 52: 263–273

Bauer HF; Eidel W (1987) Marangoni convection in a spherical liquid system. Acta Astronautica 15: 275–290

Carpenter BM; Homsy GM (1990) High Marangoni number convection in a square cavity: Part II. Phys Fluids 2: 137–149

De Gennes PG; Prost J (1993) The Physics of Liquid Crystals – 2nd ed. New York: Oxford University Press

Duda U (1993) Thermokapillare Konvektionen in sphärischen Fluidsystemen unter Gravitations-und Mikrogravitations-bedingungen. Ph.D. Thesis. University Essen

Hiller WJ; Kowalewski TA (1987) Simultaneous measurement of temperature and velocity fields in thermal convective flows. In: Flow Visualization. (ed Véret, C). Vol. 4, pp 617–622, New York: Hemisphere

Jayaraj K; Cole R; Subramanian RS (1982) Combined thermocapillary and buoyant flow in a drop in a space laboratory. J Colloid and Interface Sci 85: 66–77

Napolitano LG; Monti R; Russo G (1985) Marangoni convection in low gravity: Experiment 1 ES328, Earth-Orient. applic. Space Technol 5: 69–82

Ostrach S (1982) Low gravity fluid flows Ann Rev Fluid Mech 14: 313–345

Petri B (1990) Marangonikonvektion in Tropfen unter Mikro-gravitation. Ph.D. Thesis. University Bremen

Petri B; Delgado A; Rath HJ (1991) Thermische Marangoni-konvektion in Tropfen unter Mikrogravitation bei Beachtung der Tropfendeformation. Arch Appl Mech 61: 404–413

Saghir MZ; Choma CT (1987) Numerical simulation of thermocapillary convection inside a liquid drop, preprints of "Space bound '87". First Canadian Workshop on R&D Opportunities on Board the Space Station. May 6–8, Ottawa

Schwabe D (1981) Marangoni effects in crystal growth melts. Physico-Chemical Hydrodynamics 2: 263–280